Immobilization of the N-terminal helix stabilizes prefusion paramyxovirus fusion proteins

Albert S. Song[a,1], Taylor A. Poor[a,1], Luciano A. Abriata[b,c], Theodore S. Jardetzky[d], Matteo Dal Peraro[b,c,2], and Robert A. Lamb[a,e,2]

[a]Department of Molecular Biosciences, Northwestern University, Evanston, IL 60208-3500; [b]Institute of Bioengineering, School of Life Sciences, École Polytechnique Fédérale de Lausanne, CH-1050 Lausanne, Switzerland; [c]Swiss Institute of Bioinformatics, CH-1015 Lausanne, Switzerland; [d]Department of Structural Biology, Stanford University, Stanford, CA 94305; and [e]Howard Hughes Medical Institute, Northwestern University, Evanston, IL 60208-3500

Contributed by Robert A. Lamb, May 25, 2016 (sent for review February 19, 2016; reviewed by John Johnson and Benoît Roux)

Parainfluenza virus 5 (PIV5) is an enveloped, single-stranded, negative-sense RNA virus of the Paramyxoviridae family. PIV5 fusion and entry are mediated by the coordinated action of the receptor-binding protein, hemagglutinin–neuraminidase (HN), and the fusion protein (F). Upon triggering by HN, F undergoes an irreversible ATP- and pH-independent conformational change, going down an energy gradient from a metastable prefusion state to a highly stable postfusion state. Previous studies have highlighted key conformational changes in the F-protein refolding pathway, but a detailed understanding of prefusion F-protein metastability remains elusive. Here, using two previously described F-protein mutations (S443D or P22L), we examine the capacity to modulate PIV5 F stability and the mechanisms by which these point mutants act. The S443D mutation destabilizes prefusion F proteins by disrupting a hydrogen bond network at the base of the F-protein globular head. The introduction of a P22L mutation robustly rescues destabilized F proteins through a local hydrophobic interaction between the N-terminal helix and a hydrophobic pocket. Prefusion stabilization conferred by a P22L-homologous mutation is demonstrated in the F protein of Newcastle disease virus, a paramyxovirus of a different genus, suggesting a conserved stabilizing structural element within the paramyxovirus family. Taken together, the available data suggest that movement of the N-terminal helix is a necessary early step for paramyxovirus F-protein refolding and presents a novel target for structure-based drug design.

molecular dynamics simulation | viral fusion protein | protein refolding

The Paramyxoviridae family includes human and livestock viruses of significant clinical and economic concern, such as parainfluenza viruses (PIV) 1–5, mumps virus, measles virus, Newcastle disease virus (NDV), respiratory syncytial virus (RSV), human metapneumovirus (hMPV), and the zoonotic Hendra and Nipah viruses. With the increasing prevalence of human-to-human transmission of zoonotic Henipaviruses (1, 2) and with more than 60 novel paramyxoviruses identified in a single study (3), the growth and clinical significance of this family highlight the need for further investigation.

Paramyxoviruses are single-stranded, negative-sense RNA viruses that are enveloped by a lipid bilayer. To gain entry into a host cell, enveloped viruses need to fuse their viral membrane with a target cell membrane. Paramyxoviruses mediate this fusion event by the concerted action of two surface-expressed spike glycoproteins: the attachment protein [hemagglutinin–neuraminidase (HN), H, or G] and the fusion protein (F). Whereas the attachment protein is involved in target cell recognition, receptor binding, and triggering of F at the right time and place, the fusion protein physically mediates the pH-independent fusion of the viral and target cell membrane (4).

Paramyxovirus F proteins, along with influenza virus HA, Ebola virus GP, and HIV gp41, are class I viral fusion proteins (5). These proteins are initially synthesized as homotrimeric precursors that must be proteolytically cleaved for fusion activity (6–8) and folded into a metastable prefusion conformation. Atomic structures of paramyxovirus F proteins for PIV5, RSV, hMPV, Hendra, and Nipah viruses in the prefusion form (9–13) and hPIV3, NDV, and RSV in the postfusion form (14–16) demonstrate that the prefusion F trimer is characterized by a globular head and trihelical coiled-coil stalk that extends into the viral membrane, whereas the postfusion F trimer is characterized by a compacted globular head and stable membrane-proximal six-helix bundle (reviewed in ref. 4). Together with biochemical and structural data of paramyxovirus attachment proteins (17–28), a general model of paramyxovirus fusion has been proposed: upon activation by the attachment protein, metastable prefusion F undergoes a series of large-scale, ATP-independent conformational changes, going down an energy gradient from a metastable prefusion state to a highly stable postfusion state. The energy released during F refolding is believed to facilitate membrane fusion to create a pore between the virus and host cell through which the viral ribonucleoprotein complex can enter the target cell.

Previous experiments have probed PIV5 F to highlight key conformational changes that occur as the F protein refolds from the prefusion to postfusion state (29–32). Despite recent efforts to stabilize the prefusion state of paramyxovirus fusion proteins for vaccine development (33–35), an understanding of the metastable prefusion state and the capacity to modulate prefusion stability remains elusive. As the prefusion state is a potential vaccine target, a better understanding of the dynamic fusion protein will help guide future antiviral developments. Here, we applied site-directed mutagenesis and all-atom molecular dynamics simulations to examine the structural details of the prefusion F protein in the context of stabilizing and destabilizing mutations derived from the WR isolate

Significance

Paramyxovirus fusion proteins (F), critical for viral entry and infection, initially fold into a metastable prefusion state and, upon triggering, refold irreversibly to a stable postfusion state to physically mediate membrane fusion. The large-scale conformational changes that occur in the F-refolding pathway are understood, but a detailed structural understanding of F-protein metastability remains elusive. Here, stabilizing and destabilizing mutations of the parainfluenza virus 5 fusion protein were examined to reveal that the immobilization of the N-terminal helix stabilizes paramyxovirus prefusion F proteins. The N-terminal helix, the interaction of which with domain II appears to be a critical early step in the F-protein refolding pathway, presents a novel alternative target for structure-based antiviral therapeutics.

Author contributions: A.S.S., T.A.P., L.A.A., T.S.J., M.DP., and R.A.L. designed research; A.S.S., T.A.P., L.A.A., and M.DP. performed research; A.S.S., T.A.P., L.A.A., T.S.J., and M.DP. analyzed data; and A.S.S., T.A.P., L.A.A., T.S.J., M.DP., and R.A.L. wrote the paper.

Reviewers: J.J., The Scripps Institute; and B.R., University of Chicago.

The authors declare no conflict of interest.

[1]A.S.S. and T.A.P. contributed equally to this work.

[2]To whom correspondence may be addressed. Email: matteo.dalperaro@epfl.ch or ralamb@northwestern.edu.

This article contains supporting information online at www.pnas.org/lookup/suppl/doi:10.1073/pnas.1608349113/-/DCSupplemental.

www.pnas.org/cgi/doi/10.1073/pnas.1608349113

of PIV5 F, previously identified by Ito et al. (36). The F protein of WR PIV5 differs from that of the well-characterized W3A isolate by only two ectodomain residues. Whereas W3A F is characterized by a proline at residue 22 and serine at residue 443, WR F is characterized by a leucine at residue 22 and a proline at residue 443. Paterson et al. (37) demonstrated that mutation of each different WR F ectodomain residue into the W3A F background caused dramatically different fusion phenotypes: the P22L mutation stabilized W3A F, whereas the S443P mutation destabilized W3A F. When both P22L and S443P mutations were present in a W3A F background, the fusion activity returned to wild-type levels, suggesting that the two mutations had a compensatory effect.

Recently, we determined the atomic structure of the ectodomain of prefusion PIV5 WR F, which revealed that, compared with PIV5 W3A F, the leucine at residue 22 rotated inward and appeared to interact with a hydrophobic pocket on the side of the F globular head. We subsequently performed site-directed mutagenesis to characterize the prefusion stabilization conferred by the P22L mutation (38). Although substitutions of residue 22 by hydrophobic amino acids smaller than leucine demonstrated W3A levels of fusion activity, hydrophobic side chains equal to or larger than leucine demonstrated diminished levels of fusion activity. We concluded that prefusion stability is mediated by residue 22 in a hydrophobic size-dependent fashion. Here, by further investigating mutations at residue 22 as well as at residue 443, we demonstrate that the immobilization of the N-terminal helix of paramyxovirus F proteins confers a stabilization of the prefusion state and suggest that movement of the N-terminal helix is a necessary early step in the paramyxovirus F-protein refolding pathway.

Results

Rescue of Prefusion Stability by the P22L Mutation. Along with the prefusion PIV5 WR F structure and characterization of the P22L mutation, we previously reported on destabilizing mutations at residue 443 (38). Of particular interest was a highly destabilizing S443D mutation. As previously reported (38), cell-surface expression measured by prefusion-specific monoclonal F1a antibody binding (39) was not detected for F-S443D despite greater-than-W3A levels of fusion protein activity measured by a luciferase reporter assay and syncytia formation (Fig. 1). To better understand the conflict between low surface expression and high fusion protein activity, the expression and processing of F-S443D were tracked through a pulse label and chase experiment (Fig. S1). These data demonstrated that F-S443D synthesis and processing are comparable to that of W3A F. Together with total surface expression measured by polyclonal antibody binding (Fig. S2), we concluded that F-S443D is properly processed, but rapidly converted to the postfusion state upon arrival at the cell surface. Similar to what was seen with WR F, the introduction of P22L into a F-S443D backbone rescued prefusion stability, as detected by an increase in prefusion F-protein surface expression (Fig. 1*A*). However, F-P22L/S443D retained high fusion protein activity (Fig. 1*B*), suggesting that an aspartic acid at residue 443 is more destabilizing than a proline.

In Silico Characterization of Residues 22 and 443. The stabilizing P22L mutation has been proposed to function through local interactions between the leucine side chain and a hydrophobic pocket on the side of the F-protein globular head, whereas the destabilizing S443D mutation has been suggested to function by disrupting a local hydrogen bond network at the base of the F-protein globular head (38) (Fig. 2*A*, *Right* and *Left Inset*, respectively). However, it is not clear how these point mutations exert global, long-range forces to stabilize or destabilize prefusion PIV5 F. To explore the network of functionally important interactions within PIV5 F, we performed 110- to 140-ns-long all-atom molecular dynamics simulations on four F-protein constructs—W3A F, F-P22L, F-S443D, and F-P22L/—using the trimeric, cleaved, prefusion PIV5 W3A F structure as our starting model (PDB ID code 4GIP) (40). Our simulations

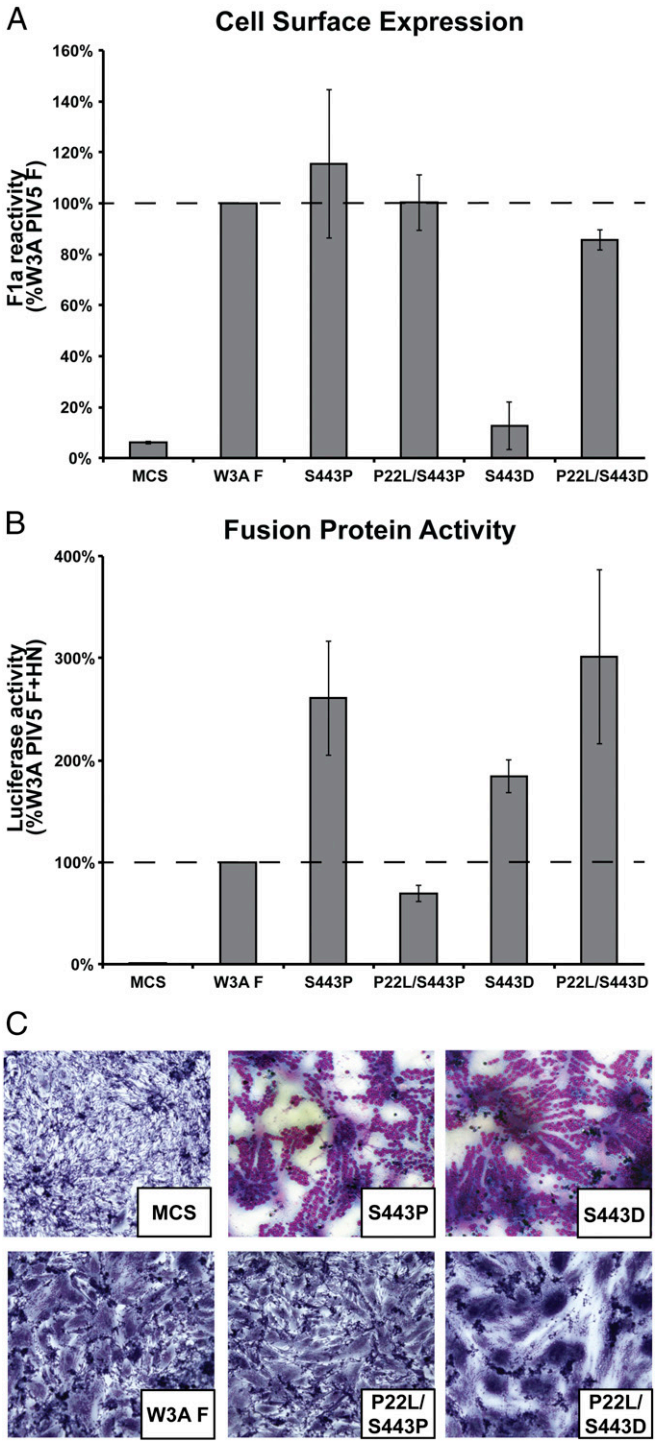

Fig. 1. Rescue of prefusion stability by the P22L mutation. (*A*) Prefusion F-protein surface expression was detected by flow cytometry using a prefusion-specific monoclonal antibody, F1a. MFI values were calculated and normalized against wild-type W3A F. (*B*) Fusion activity was quantified using a luciferase reporter assay and normalized against wild-type W3A F+HN fusion activity. The rescue of fusion protein stability manifests either through increased surface expression as detected in *A* or through decreased fusion protein activity as detected in *B*. (*C*) F-protein activity was visualized through syncytia formation of transfected BHK-21 cells. Cells were fixed and stained 18 h posttransfection. All experiments were done in triplicate and error bars represent ±1 SD. S443P and S443D data were described previously (38). (Magnification: 160×.)

support the mechanisms of action proposed for the P22L and S443D mutations. We observed (*i*) shorter distance and a larger number of hydrophobic contacts between the N-terminal helix and the hydrophobic pocket for F-P22L and F-P22L/S443D compared with W3A F and F-S443D (Fig. 2 *B* and *C*, respectively) and (*ii*) a lower number of hydrogen bonds established by Asp443 in F-S443D and F-P22L/S443D compared with Ser443 in W3A F and F-P22L (Fig. S3*B*).

None of the four simulations engages any large-scale conformational changes like those involved in F refolding, most likely because of the large system size and long timescales necessary for such conformational changes. Instead, the proteins in the four simulations remain close to the starting conformation (Fig. S4). However, long-range mechanical couplings of potential functional relevance around the starting conformation can still be investigated by computing dynamic cross-correlation maps (DCCM) from the trajectories (41–44). DCCMs highlight pairs of residues that undergo correlated motions, including "trivial" pairs of residues that are covalently linked or spatially adjacent and functionally more interesting pairs of distant residues that are mechanically coupled over large distances.

The DCCM (Fig. 3*A* and Fig. S5) summarizes the extent of mechanical coupling between all possible residue pairs in W3A F. By averaging correlations within and between domains of each protomer, we noticed that domains I and II are more correlated with each other than with domain III (see circles in Fig. 3*A* and Fig. S5*B*). Mapped in Fig. 3 *A* and *B*, the strongest correlations between domains I and III occurred between residues 324 and 336 (light and dark green spheres) of domain I and residues 116 and 127 (white spheres), 217 and 225 (dark gray spheres), and 248 and 257 (black spheres) of domain III. Notably, many of these residues lie beneath the β-strap, a previously described structure (29) that connects domains I and III and is defined by two β-strands composed of residues G29 to K52 and T256 to T291 in PIV5 F.

We can further highlight changes in global protein dynamics exerted by each mutation by computing the differences in correlation between W3A F and the mutant constructs. To simplify visualization, we selected "probe" residues and mapped the changes in correlation onto the prefusion PIV5 F structure. Each probe residue acts as the central reference point against which the correlations to motions of all other residues are calculated. Residues with motions more correlated to motions of the probe residue are depicted as redder, thicker tubes in Fig. 3 *C*–*E*. For example, the introduction of P22L

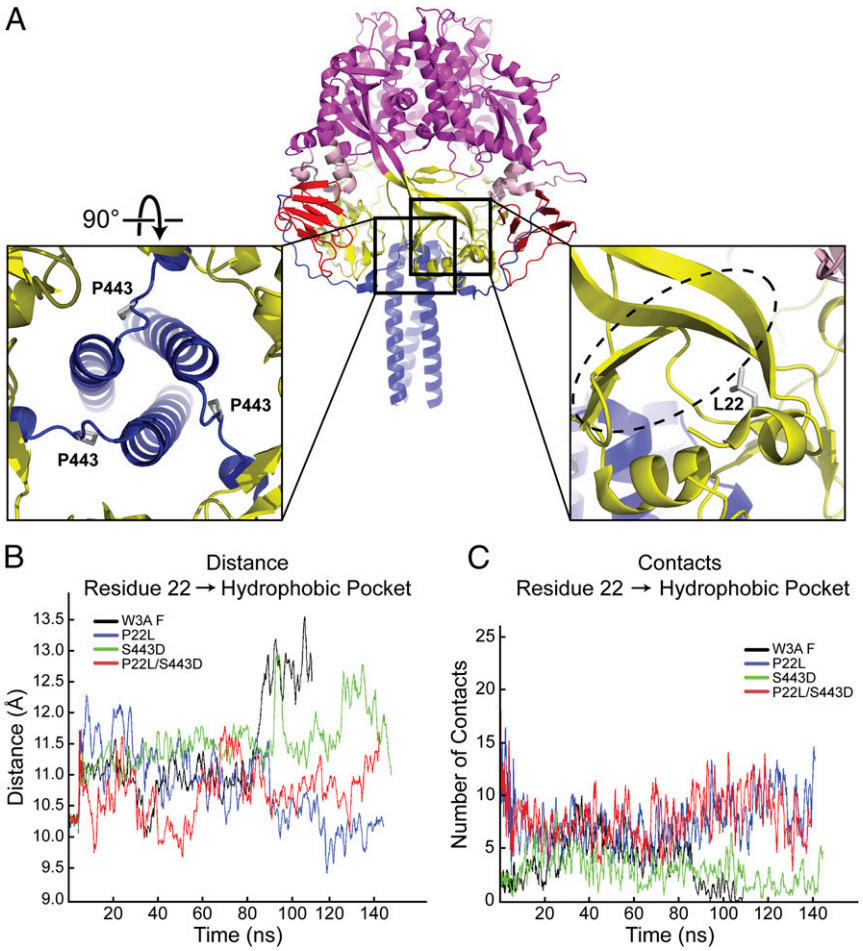

Fig. 2. Topology of PIV5 WR F and effect of mutations on the stability of a hydrophobic pocket around residue 22. (*A*) Cartoon representation of the prefusion PIV5 WR F structure (PDB ID code 4WSG) with domains colored as described previously (9). *Insets* on the *Left* and *Right* highlight the structural elements surrounding S443P and P22L, respectively, which are represented as gray sticks in the mutated form (Pro443 and Leu22). The hydrophobic pocket is highlighted by a dashed oval in the *Inset* on the *Right*. (*B*) Distance of residue 22 from the hydrophobic pocket in W3A F, F-P22L, F-S443D, and F-P22L/S443D simulations. The presence of P22L decreases distance between the N-terminal helix and the hydrophobic pocket. (*C*) The number of hydrophobic contacts between residue 22 and the hydrophobic pocket. The introduction of P22L increases the number of hydrophobic contacts between the N-terminal helix and the hydrophobic pocket. Distance and contact measurements are a frame-wise average of the three protomers. A moving average filter with a 1-ns window was applied for better visualization.

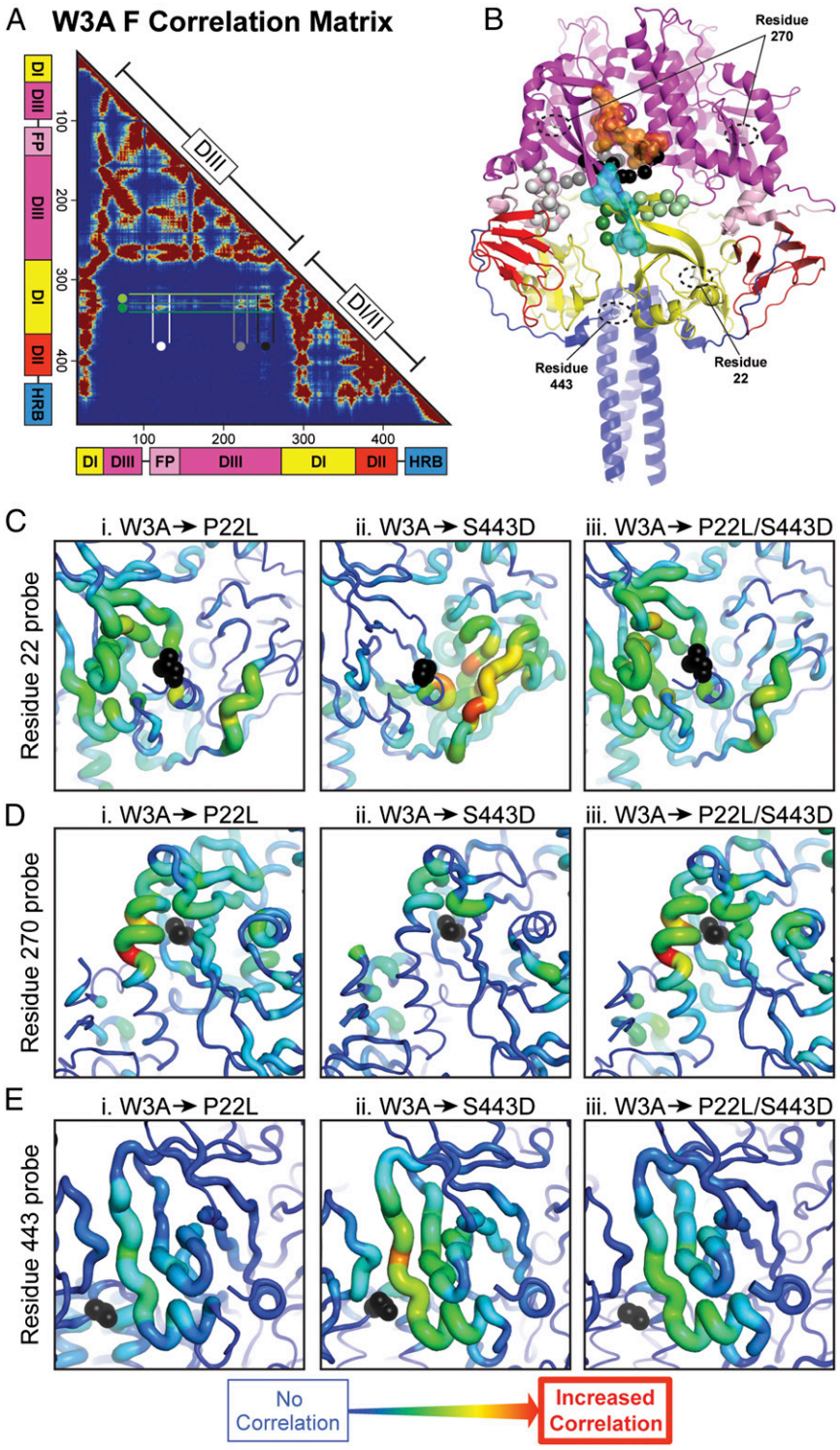

Fig. 3. Dynamic cross-correlation map and analysis of fusion protein simulations. (*A*) Cross-correlation coefficients were mapped between all possible residue pairs within one protomer of W3A F throughout the simulation. Only positive coefficients, where values range from 0 for completely uncorrelated motions (blue) to 1 for perfectly correlated motions (red), are shown. Correlated motions indicate regions of the protein whose internal mechanics are coupled either through direct short-range contacts or long-range interactions. Correlation coefficients greater than 0.1 between domain I and domain III are boxed and marked with circles. (*B*) Cartoon representation of PIV5 WR F colored according to the domain diagram in *A*. DI/DIII-correlated residues identified in *A* are shown as colored spheres. The epitopes of anti-RSV F antibodies (MPE8 in cyan, Palivizumab in orange) are mapped onto PIV5 F as translucent surfaces. Residues used as probes in *C*–*E* are depicted as sticks and highlighted by dashed circles. (*C*–*E*) For all F-protein mutants, the change in correlation compared with the W3A F simulation (difference of absolute values to highlight changes in overall correlation strengths) was measured using a probe at residue 22, 270, or 443 (black spheres), respectively. Stronger correlated motions compared with W3A F are shown as thicker, redder putty, whereas weaker correlated motions are shown as thinner, bluer putty. The tubing size/color variation represents a correlation coefficient difference range of 0–0.075.

increased correlation between residue 22 and the hydrophobic pocket compared with W3A F (Fig. 3 *C, i*), whereas S443D increased correlation between residue 22 and the β-sheets of domain II (Fig. 3*Cii*). The double-mutant F-P22L/S443D displayed increased correlation in a pattern most similar to F-P22L (Fig. 3 *C*, *iii*, same pattern as Fig. 3 *C*, *i*).

Long-distance effects of the P22L mutation were also seen between the fusion peptide and the β-strap. Using residue V270 in the β-strap as a probe (selected based on cross-correlation data and for its proximity to the fusion peptide), the presence of P22L increased correlation of the fusion peptide with the side of the globular head (Fig. 3 *D*, *i* and *ii*). As the release of the fusion peptide is an absolute requirement for proper F-protein function, this observation suggests an additional, long-distance mechanism for P22L stabilization of the prefusion state.

Using residue 443 as the probe, we also noted increased correlation with the hydrophobic pocket in the presence of the S443D mutation (Fig. 3 *E*, *ii* and *iii*). The majority of this increased correlation appeared to arise from the α-helix that comprises the base of the hydrophobic pocket. The correlation profile of the double-mutant F-P22L/S443D (Fig. 3 *E*, *iii*) appears to be an intermediate of F-P22L (Fig. 3 *E*, *i*) and F-S443D (Fig. 3 *E*, *ii*).

The P22L Mutation Robustly Rescues Prefusion F-Protein Stability. As previously noted, the top of heptad repeat B (HRB) and an adjacent α-helix from domain I are believed to participate in a hydrogen bond network that is critical for prefusion stability (9, 38). Although it has been proposed that disruption of this network by destabilizing mutations at residue 443 leads to a hyperfusogenic phenotype, the simulations suggest, as described above, that the destabilizing S443D mutation is unexpectedly more correlated with the α-helix and the hydrophobic pocket. To investigate the structural relationships between the α-helix, the hydrogen bond network, and the N terminus, we identified and mutated the other residues predicted to participate in the network (S342, T345, D448, and Q451) (Fig. 4*A*, *Inset*), measured their fusion phenotypes, and attempted to rescue prefusion stability through the addition of P22L.

Similar to hyperfusogenic mutations created at the protomer–protomer interface for multiple paramyxoviruses (20, 45, 46), all mutations created at the protomer–promoter interface between the α-helix and HRB stalk demonstrated varying degrees of destabilization (Fig. 4 *B* and *C*). As described for Ser443 mutations in Fig. 1, destabilization can manifest as high levels of fusion protein activity with either low or W3A levels of prefusion surface expression (e.g., F-T345A and F-D448A, respectively). Furthermore, for all destabilized mutant constructs, the introduction of P22L robustly rescued prefusion stability. For example, in constructs such as F-D448A, where destabilization manifests as wild-type levels of prefusion surface expression, the addition of P22L abolished fusion protein activity. In constructs where destabilization manifests as low prefusion surface expression, such as F-D448A/Q451A, the addition of P22L restored prefusion surface expression to W3A F levels. Mutations that had low levels of expression by prefusion-specific monoclonal antibody binding were confirmed to have W3A F levels of expression by polyclonal antibody binding (Fig. S2), suggesting that the mutations are not interfering with protein expression or folding.

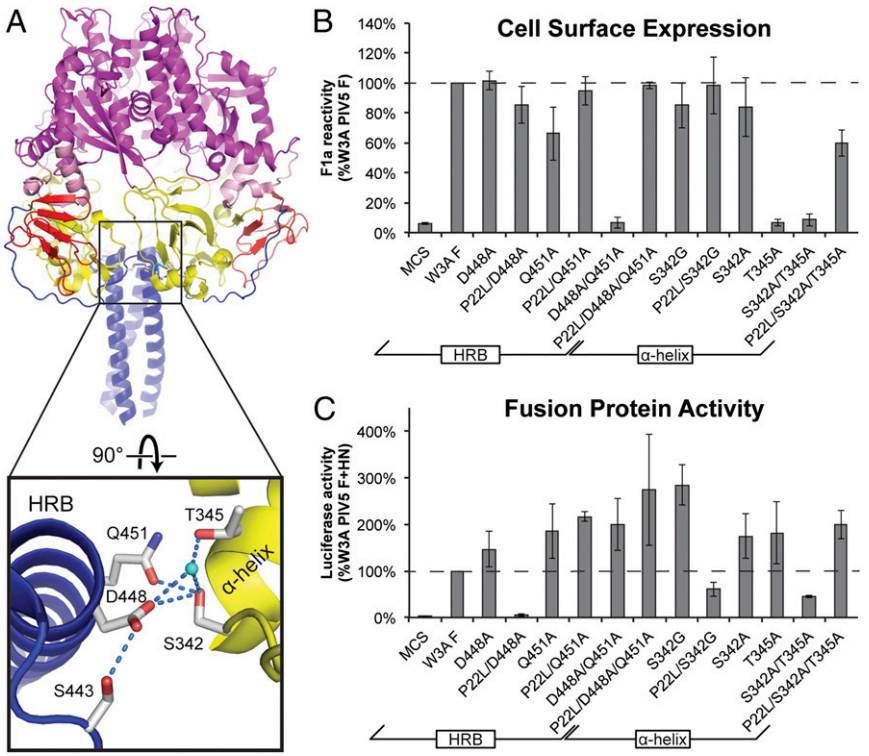

Fig. 4. Prefusion stabilization by the P22L mutation is robust. (*A*) Cartoon representation of the cleaved prefusion PIV5 F structure (PDB ID code 4GIP) and configuration of the hydrogen bond network (*Inset*). Hydrogen bonds are represented by blue dashes and an ordered water is represented by a cyan sphere. (*B*) Prefusion F-protein surface expression was detected by flow cytometry using a prefusion-specific monoclonal antibody, F1a. MFI values were calculated and normalized against wild-type W3A F. (*C*) F-protein fusion activity was quantified using a luciferase reporter system and normalized against wild-type W3A F+HN fusion activity. For all mutant proteins, the rescue of fusion protein stability by the introduction of the P22L mutation manifests either through increased surface expression as detected in *A*, decreased fusion protein activity as detected in *B*, or a combination of the two. All experiments were done in triplicate and error bars represent ±1 SD.

The P22L-homologous Mutation in NDV F Demonstrates a Rescue Phenotype. To test whether prefusion stabilization conferred by the P22L mutation can be generalized to other paramyxoviruses, a P22L-homologous mutation was made in the fusion protein of the Newcastle disease virus (NDV F-G34L). Similar to that of PIV5 F-P22L, NDV F-G34L was surface-expressed at wild-type levels and demonstrated a stabilized fusion phenotype (Fig. 5). To test whether the addition of G34L could also rescue prefusion stability, G34L was mutated into the backbone of a previously characterized hyperfusogenic NDV F-L289A (47). The G34L mutation was indeed able to rescue prefusion NDV F-L289A stability, demonstrated by decreased fusion activity in both a luciferase reporter assay and syncytia formation (Fig. 5 *B* and *C*).

Discussion

Fusion of the viral membrane with a host cell membrane is an absolute requirement for infection by enveloped viruses. As the physical mediator of viral membrane fusion, the F protein is an attractive target for antiviral therapeutics. However, the large size and metastability of the F protein make it difficult to study. Here, we investigated the malleable metastability of the prefusion PIV5 W3A F protein through site-directed mutagenesis and atomistic molecular dynamics simulations.

We extended our previous findings (38) to demonstrate that a single N-terminal point mutation, P22L, robustly stabilizes the PIV5 F prefusion state for a disparate array of destabilizing mutations (Figs. 1 and 4, with point mutation data summarized in Table S1). A novel P22L-homologous mutation (NDV F-G34L) also rescues prefusion stability of the F protein of NDV, a member of a different paramyxovirus genus (Fig. 5). Supported by MD simulations of four F-protein constructs—W3A F, F-P22L, F-S443D, and F-P22L/S443D—this P22L mutation appears to function by increasing interactions between the N-terminal helix and a hydrophobic pocket of domain I (Figs. 2 and 3*C* and Fig. S3). As measured by changes in global protein dynamics, P22L also appears to exert local forces that propagate through covalent and noncovalent interactions to reach distant regions (~30 Å), most notably including the fusion peptide (Fig. 3*D*). Successful stabilization of prefusion RSV F protein using cavity-filling hydrophobic substitutions or hinge-movement–inhibiting mutations in the same region of the protein as PIV5 F-V270 have been reported previously (34). The obvious structural link connecting residue 22, the hydrophobic pocket, and the fusion peptide is the β-strap that runs along the side of the globular head. The NDV F L289A mutation (Fig. 5) and pairs of residues with the strongest correlation between domains I and III (highlighted in Fig. 3 *A* and *B*) are located in the β-strap. As the target of a broadly neutralizing antibody in RSV and hMPV (MPE8 epitope highlighted by the cyan surface and Palivizumab epitode highlighted by orange surface in Fig. 3*B*) (10, 48), and a region that experiences a dramatic reduction in conformational flexibility during PIV5 F-protein refolding (29), this β-strap appears to be a critical structural motif in the proper function of the F protein.

Conversely, the destabilizing S443D mutation appears to function by disrupting a hydrogen bond network at the base of the F-protein globular head (38) (Fig. S3). As measured by changes in global protein dynamics, the S443D mutation alone promotes mechanical coupling between the N terminus and domain II (Fig. 3*C*). As domain II was previously identified as a critical site for F-activation by HN (49, 50), F-S443D's increase in mechanical coupling between the N terminus and domain II may suggest a functionally critical interaction during the F-protein refolding pathway.

Previously, binding of the 05D synthetic antibody (sAb) to the PIV5 F N-terminal region (51) was demonstrated to block viral fusion and hypothesized to function either by stabilizing the prefusion F protein or blocking F–HN interaction. Similarly, the human metapneumovirus F-neutralizing antibody, DS7, was determined to target the N-terminal region and neutralize the prefusion state without generating escape mutants, despite the antigen site being structurally

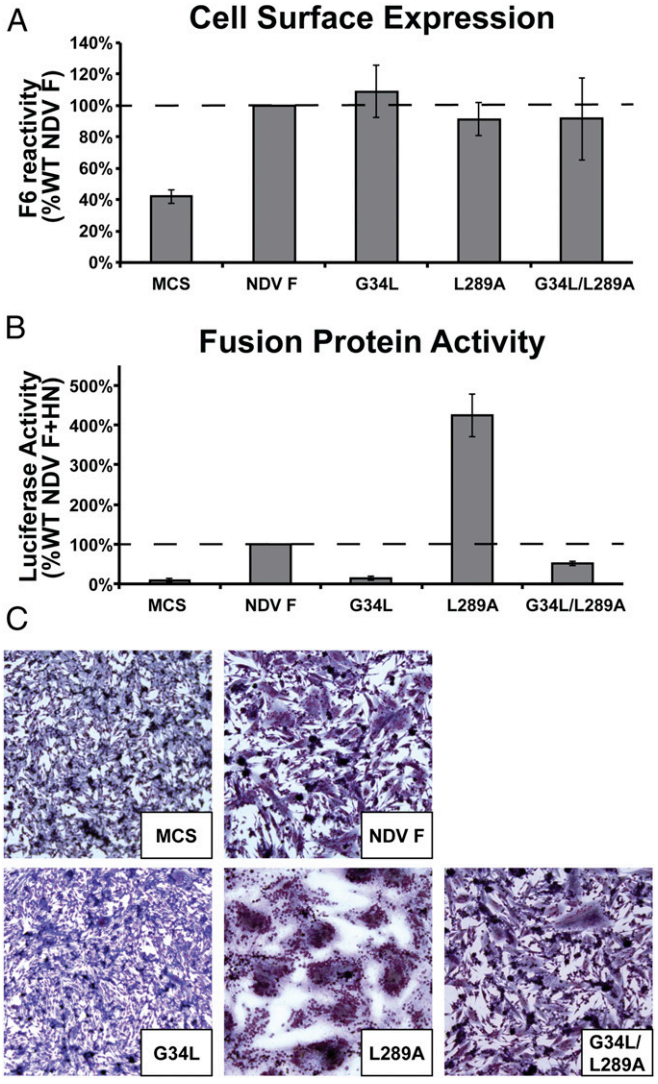

Fig. 5. A conserved mechanism of paramyxovirus prefusion F stability. (*A*) Prefusion NDV F-protein surface expression was detected by flow cytometry using a NDV F polyclonal antibody, F6. MFI values were calculated and normalized against wild-type NDV F. (*B*) NDV F-protein fusion activity was quantified using a luciferase reporter assay and normalized against wild-type NDV F+HN fusion activity. The rescue of fusion protein stability by a PIV5 P22L-homologous mutation, NDV F-G34L, manifests through decreased fusion protein activity. All experiments were done in triplicate and error bars represent ±1 SD. (*C*) NDV F-protein activity was visualized through syncytia formation of transfected BHK-21 cells. Cells were fixed and stained 18 h posttransfection. (Magnification: 160×.)

invariant between the prefusion and postfusion states (10). Based on data shown here, we hypothesize that the 05D sAb and the DS7 Fab immobilize the N-terminal helix to stabilize hMPV F proteins in the prefusion conformation.

Here, we suggest that movement of the N-terminal helix is a necessary early step in the paramyxovirus F-protein refolding pathway and that the effect of P22L in PIV5 F (and G34L in NDV F) is mediated through the β-strap to stabilize the fusion peptide against the globular head in the prefusion conformation. Given that the hydrophobic pocket appears to be a conserved structural feature in the available atomic structures of paramyxovirus F proteins, the N-terminal helix and the hydrophobic pocket of paramyxovirus F proteins present an alternative avenue of investigation for structure-based rational drug design.

Materials and Methods

Mammalian Cells and Expression of F and HN Glycoproteins. Vero cells were maintained in Dulbecco's Modified Eagle's Medium (Life Technologies) supplemented with 10% (vol/vol) FBS and 1% penicillin/streptomycin. BSR-T7/5 and BHK-21 cells were maintained in Dulbecco's Modified Eagle's Medium (Life Technologies) supplemented with 10% FBS, 10% tryptose phosphate broth, and 1% penicillin/streptomycin. BSR-T7/5 cells were grown with G418 added every third passage. All percentages reflect volume-per-volume calculations. PIV5 F and HN as well as NDV F and HN were expressed in Vero, BHK-21, and HEK 293T cells by transient transfection of the pCAGGS-F and pCAGGS-HN using the Lipofectamine Plus transfection reagents (Invitrogen), according to the manufacturer's protocol. Transfections were prepared in OPTIMEM media and added dropwise to the cells. Samples were incubated overnight in a 37 °C/5% CO_2 incubator.

Cloning and Mutagenesis. pCAGGS-F and pCAGGS-HN expression constructs harboring the PIV5 W3A F and HN or NDV F and HN (strain Australia-Victoria) genes were used as described previously (19, 50). Mutations in pCAGGS-F were constructed by four-primer PCR. The PCR fragment was digested using KpnI and SacI and ligated into a pCAGGS vector. The sequence of each mutant F protein was verified using an Applied Biosystems 3100-Avant automated DNA sequencer (Life Technologies). pT7-luciferase was obtained from Promega.

Cell-Surface Expression Measured by Flow Cytometry. Human Embryonic Kidney (HEK) 293T cells were transfected with 2 μg of plasmid encoding PIV5 F or NDV F protein as described above. Eighteen hours posttransfection, the monolayers were washed 1× with PBS^- containing 0.02% sodium azide. To prevent nonspecific antibody binding, 0.5 mL of PBS^- containing 0.02% sodium azide and 1% BSA was added and cells were rocked at 4 °C for 30 min. The blocking solution was removed and 0.5 mL of primary antibody [prefusion, cleavage-activated PIV5 F-specific monoclonal F1a antibody, PIV5 F polyclonal R9176 antibody (raised in rabbits against purified PIV5 F protein ectodomain), or NDV F polyclonal F6 antibody, diluted 1:100 in PBS^- containing 0.02% sodium azide and 1% BSA] was added. Samples with primary antibody were rocked for 1 h at 4 °C. Monolayers were washed 5× with PBS^- containing 0.02% sodium azide and 0.5 mL of secondary antibody [fluorescein isothiocyanate (FITC)-conjugated IgG goat–α-mouse secondary antibody or FITC-conjugated IgG goat–α-rabbit secondary antibody (Jackson ImmunoResearch) diluted 1:100 in PBS^- containing 0.02% sodium azide and 1% BSA] was added. Samples with secondary antibody were rocked for 1 h at 4 °C. Secondary antibody was removed and the cells were washed 5× as before. PBS^- (0.5 mL) was added to each sample and resuspended in 0.5 mL of PBS^- containing 1% formaldehyde. The mean fluorescence intensity (MFI) of 100,000 cells was recorded for each sample using a FACSCanto II flow cytometer (Becton, Dickinson). Flow cytometry data were collected using the FACSDiva software (Becton, Dickinson) and analyzed using FCSExtract software (Stowers Institute for Medical Research).

Syncytium Formation. BHK-21 cells were transfected with 1 μg each of plasmid encoding PIV5 F and HN or NDV F and HN as described above. Eighteen hours posttransfection, cells were washed with PBS^+, fixed and stained using the Hema3 solution (Fisher Scientific) according to the manufacturer's protocol, and imaged to determine syncytia formation. Images are representative of three independent experiments. Auto-contrast, tone, and brightness adjustments were applied to all images equally (batch processed) using Adobe Photoshop.

Luciferase Reporter Fusion Assay. To quantitate fusion observed in syncytia formations, Vero cell monolayers were transfected with 1 μg each of plasmid encoding PIV5 F and HN or NDV F and HN as described above. pT7 luciferase, a plasmid that expresses firefly luciferase under control of the T7 RNA polymerase, was added to all samples. BSR-T7/5 (a BHK clone stably expressing T7 polymerase) cells were overlaid on the Vero cell monolayer at 16 h posttransfection and incubated for 8 additional hours at 37 °C/5% CO_2 to allow expression of the luciferase protein. After washing 1× with PBS^+, Glo-lysis buffer (Promega) was used to lyse the cells. Cell debris was removed by centrifugation (13,000 × *g* for 3 min), and 150 μL of sample along with 150 μL of luciferin substrate (Promega) was added to a 96-well plate. Luciferase activity in relative light units was determined using a SpectraMax M5 plate reader (Molecular Devices).

Pulse Label and Chase. HeLa cells were plated onto 6-cm tissue culture dishes (Sarstedt) and transfected with 1 μg of pCAGGS W3A F, pCAGGS S443D F, or empty pCAGGS vector (MCS) as described above. At 16 h posttransfection, the cells were washed 3× with PBS^+ and starved for 30 min with 3 mL of DMEM lacking cysteine and methionine. After 30 min, the medium was replaced with 1 mL of DMEM (lacking cysteine and methionine) supplemented with [^{35}S]-Promix (50 μCi per dish) and returned to 37 °C/5% CO_2 for 20 min (the "pulse"). After 20 min, the radioactive DMEM was aspirated, replaced with 5 mL of "chase" media (DMEM + 10% FBS + 1% penicillin/streptomycin), and incubated at 37 °C/5% CO_2 for 0, 15, 30, 45, 60, and 90 min. The control dishes were stopped at 0 and 90 min chase. At each time point, cells were transferred to ice to minimize protease activity, washed 2× with PBS^-, and lysed using 1 mL of 1× radioimmunoprecipitation assay (RIPA) buffer (52) supplemented with protease inhibitors, 1 mM phenylmethylsulfonyl fluoride, and 10 mM iodoacetamide. The cell lysate was clarified by ultracentrifugation at 55,000 rpm in a Beckman TLX ultracentrifuge with a TLA 120.2 rotor at 4 °C for 10 mins, transferred to a 1.5-mL Eppendorf tube, and kept on ice. Primary antibody (α-PIV5 F rabbit polyclonal R9176) was added at a 1:100 dilution, and samples were rocked for 2 h at 4 °C. After primary antibody binding, 35 μL of protein A Sepharose was added to each sample and samples were rocked for 30 min at 4 °C. The beads were pelleted using a tabletop centrifuge and washed 3× with RIPA buffer containing 0.3 M NaCl, 2× with RIPA buffer containing 0.15 M NaCl, and 1× with a 50 mM Tris·HCl (pH 7.4), 0.25 mM EDTA, 0.15 M NaCl solution. Proteins were eluted from beads by boiling for 3 min in protein lysis buffer containing 15% DTT and analyzed by SDS/PAGE electrophoresis on a 15% polyacrylamide gel. Radioactivity was detected using a Fuji FLA-5100 image reader with Multi Gauge v3.0 software (Fuji Medical Systems).

Molecular Dynamics Simulations and Analysis. The crystal structure of the cleaved prefusion W3A isolate of PIV5 F (PDB ID code 4GIP) was used as the initial structure (40). Each construct of over 223,500 atoms (including the F-protein trimer, water, and neutralizing ions) was prepared for simulations using the PyMol mutagenesis tool (53) and Leap module of AmberTools (54). Simulations were run with the NAMD engine (55) using the AMBER99SB force field (56) and TIP3P parameters for water (57). Standard sodium and chloride parameters from the AMBER force field were used and glycosylations were removed for the simulations. A conservative cutoff of 12 Å (58) was set for nonbonded interactions with a switching function active between 10 Å and 12 Å. Electrostatics were treated through particle-mesh Ewald summations with a grid spacing of 1 Å. Each simulation box was minimized, equilibrated by Cα-restrained heating in 10 steps of 30 K up to 300 K for a total of 1 ns, and further equilibrated by unrestrained heating. Subsequently, the production simulations were carried out at 300 K and 1 atm, controlled with a Nosé–Hoover Langevin piston.

Trajectories were analyzed with VMD software modules and custom MATLAB and Tcl scripts. The rmsd was plotted from aligned trajectories (Fig. S5). Distance and contact measurements were calculated using VMD plugins. For distance measurements between the N-terminal helix and the hydrophobic pocket, α-carbon coordinates of residue 22 and residue 287 were used, where residue 287 was determined to be the center of mass of the hydrophobic pocket, which remains well-defined throughout the simulation as well as among prefusion and postfusion structures (9–16). For hydrophobic contact measurements, a cutoff distance of 4 Å between carbon atoms was used. For hydrogen bond contact measurements, residue 443 could act as a hydrogen bond donor or acceptor; a cutoff distance of 3.5 Å and an angle cutoff of 30° were used.

Dynamic cross-correlation maps were calculated on the Cartesian coordinates of Cα atoms after aligning the trajectories to remove the effects of translation and rotation, using a custom VMD script described previously (59). Subsequent data analysis was performed in MATLAB. The cross-correlation values were all well converged, with overlap coefficients above 0.99 computed as described by Hess (60). Only 15% of the coefficients were negative, 96% of which ranged from 0 to −0.015. The most negative value was −0.035. To calculate correlation differences among F-protein mutant simulations, absolute values of coefficient matrices were subtracted, and all coefficients relative to a single residue (e.g., residue 22, 270, or 443) were extracted for each protomer. These difference coefficient vectors, relative to a single residue within each protomer, were averaged across the three protomers and used to replace B-factor values in prefusion PIV5 F-protein structures (PDB ID codes 2B9B, 4GIP, and 4WSG) (9, 38, 40).

ACKNOWLEDGMENTS. This study was supported in part by the ThinkSwiss Research Fellowship and EPFL Summer Research Program (to A.S.S.); National Institutes of Health Training Programs Cell and Molecular Basis of Disease Grant T32-GM008061 (to T.A.P.); Viral Replication Grant T32-AI-060523 (to T.A.P.); Northwestern University's Medical Scientist Training Program Grant T32-GM008152 (to T.A.P.); and National Institutes of Health Grants AI-23173 (to R.A.L.) and GM-61050 (to T.S.J.). L.A.A. thanks EMBO and the Marie Curie Actions for a Long-Term Postdoctoral Fellowship. The M.DP. laboratory is supported by the EPFL and the Swiss National Science Foundation. R.A.L. is an Investigator of the Howard Hughes Medical Institute.

1. Luby SP, Gurley ES, Hossain MJ (2009) Transmission of human infection with Nipah virus. *Clin Infect Dis* 49(11):1743–1748.
2. Daszak P, et al. (2013) Interdisciplinary approaches to understanding disease emergence: The past, present, and future drivers of Nipah virus emergence. *Proc Natl Acad Sci USA* 110(Suppl 1):3681–3688.
3. Drexler JF, et al. (2012) Bats host major mammalian paramyxoviruses. *Nat Commun* 3(796):796.
4. Bose S, Jardetzky TS, Lamb RA (2015) Timing is everything: Fine-tuned molecular machines orchestrate paramyxovirus entry. *Virology* 479–480(60th Anniversary Issue): 518–531.
5. Harrison SC (2015) Viral membrane fusion. *Virology* 479–480:498–507.
6. Scheid A, Choppin PW (1974) Identification of biological activities of paramyxovirus glycoproteins. Activation of cell fusion, hemolysis, and infectivity of proteolytic cleavage of an inactive precursor protein of Sendai virus. *Virology* 57(2):475–490.
7. Homma M, Ouchi M (1973) Trypsin action on the growth of Sendai virus in tissue culture cells. 3. Structural difference of Sendai viruses grown in eggs and tissue culture cells. *J Virol* 12(6):1457–1465.
8. Nagai Y, Klenk H-D, Rott R (1976) Proteolytic cleavage of the viral glycoproteins and its significance for the virulence of Newcastle disease virus. *Virology* 72(2):494–508.
9. Yin HS, Wen X, Paterson RG, Lamb RA, Jardetzky TS (2006) Structure of the parainfluenza virus 5 F protein in its metastable, prefusion conformation. *Nature* 439(7072): 38–44.
10. Wen X, et al. (2012) Structure of the human metapneumovirus fusion protein with neutralizing antibody identifies a pneumovirus antigenic site. *Nat Struct Mol Biol* 19(4):461–463.
11. McLellan JS, et al. (2013) Structure of RSV fusion glycoprotein trimer bound to a prefusion-specific neutralizing antibody. *Science* 340(6136):1113–1117.
12. Xu K, et al. (2015) Crystal structure of the pre-fusion Nipah virus fusion glycoprotein reveals a novel hexamer-of-trimers assembly. *PLoS Pathog* 11(12):e1005322.
13. Wong JJ, Paterson RG, Lamb RA, Jardetzky TS (2016) Structure and stabilization of the Hendra virus F glycoprotein in its prefusion form. *Proc Natl Acad Sci USA* 113(4): 1056–1061.
14. Yin HS, Paterson RG, Wen X, Lamb RA, Jardetzky TS (2005) Structure of the uncleaved ectodomain of the paramyxovirus (hPIV3) fusion protein. *Proc Natl Acad Sci USA* 102(26):9288–9293.
15. Swanson K, et al. (2010) Structure of the Newcastle disease virus F protein in the post-fusion conformation. *Virology* 402(2):372–379.
16. McLellan JS, Yang Y, Graham BS, Kwong PD (2011) Structure of respiratory syncytial virus fusion glycoprotein in the postfusion conformation reveals preservation of neutralizing epitopes. *J Virol* 85(15):7788–7796.
17. Bishop KA, et al. (2008) Residues in the stalk domain of the Hendra virus G glycoprotein modulate conformational changes associated with receptor binding. *J Virol* 82(22): 11398–11409.
18. Melanson VR, Iorio RM (2004) Amino acid substitutions in the F-specific domain in the stalk of the Newcastle disease virus HN protein modulate fusion and interfere with its interaction with the F protein. *J Virol* 78(23):13053–13061.
19. Bose S, Song AS, Jardetzky TS, Lamb RA (2014) Fusion activation through attachment protein stalk domains indicates a conserved core mechanism of paramyxovirus entry into cells. *J Virol* 88(8):3925–3941.
20. Bose S, et al. (2011) Structure and mutagenesis of the parainfluenza virus 5 hemagglutinin-neuraminidase stalk domain reveals a four-helix bundle and the role of the stalk in fusion promotion. *J Virol* 85(24):12855–12866.
21. Bose S, et al. (2012) Fusion activation by a headless parainfluenza virus 5 hemagglutinin-neuraminidase stalk suggests a modular mechanism for triggering. *Proc Natl Acad Sci USA* 109(39):E2625–E2634.
22. Welch BD, et al. (2013) Structure of the parainfluenza virus 5 (PIV5) hemagglutinin-neuraminidase (HN) ectodomain. *PLoS Pathog* 9(8):e1003534.
23. Yuan P, Paterson RG, Leser GP, Lamb RA, Jardetzky TS (2012) Structure of the ulster strain newcastle disease virus hemagglutinin-neuraminidase reveals auto-inhibitory interactions associated with low virulence. *PLoS Pathog* 8(8):e1002855.
24. Yuan P, et al. (2011) Structure of the Newcastle disease virus hemagglutinin-neuraminidase (HN) ectodomain reveals a four-helix bundle stalk. *Proc Natl Acad Sci USA* 108(36):14920–14925.
25. Liu Q, et al. (2013) Unraveling a three-step spatiotemporal mechanism of triggering of receptor-induced Nipah virus fusion and cell entry. *PLoS Pathog* 9(11):e1003770.
26. Crennell S, Takimoto T, Portner A, Taylor G (2000) Crystal structure of the multifunctional paramyxovirus hemagglutinin-neuraminidase. *Nat Struct Biol* 7(11):1068–1074.
27. Lawrence MC, et al. (2004) Structure of the haemagglutinin-neuraminidase from human parainfluenza virus type III. *J Mol Biol* 335(5):1343–1357.
28. Bowden TA, et al. (2008) Structural basis of Nipah and Hendra virus attachment to their cell-surface receptor ephrin-B2. *Nat Struct Mol Biol* 15(6):567–572.
29. Poor TA, et al. (2014) Probing the paramyxovirus fusion (F) protein-refolding event from pre- to postfusion by oxidative footprinting. *Proc Natl Acad Sci USA* 111(25): E2596–E2605.
30. Russell CJ, Jardetzky TS, Lamb RA (2001) Membrane fusion machines of paramyxoviruses: Capture of intermediates of fusion. *EMBO J* 20(15):4024–4034.
31. Russell CJ, Kantor KL, Jardetzky TS, Lamb RA (2003) A dual-functional paramyxovirus F protein regulatory switch segment: Activation and membrane fusion. *J Cell Biol* 163(2):363–374.
32. Kim YH, et al. (2011) Capture and imaging of a prehairpin fusion intermediate of the paramyxovirus PIV5. *Proc Natl Acad Sci USA* 108(52):20992–20997.
33. Stewart-Jones GB, et al. (2015) A cysteine zipper stabilizes a pre-fusion F glycoprotein vaccine for respiratory syncytial virus. *PLoS One* 10(6):e0128779.
34. McLellan JS, et al. (2013) Structure-based design of a fusion glycoprotein vaccine for respiratory syncytial virus. *Science* 342(6158):592–598.
35. Krarup A, et al. (2015) A highly stable prefusion RSV F vaccine derived from structural analysis of the fusion mechanism. *Nat Commun* 6:8143.
36. Ito M, et al. (1997) Role of a single amino acid at the amino terminus of the simian virus 5 F2 subunit in syncytium formation. *J Virol* 71(12):9855–9858.
37. Paterson RG, Russell CJ, Lamb RA (2000) Fusion protein of the paramyxovirus SV5: Destabilizing and stabilizing mutants of fusion activation. *Virology* 270(1):17–30.
38. Poor TA, et al. (2015) On the stability of parainfluenza virus 5 F proteins. *J Virol* 89(6): 3438–3441.
39. Randall RE, Young DF, Goswami KKA, Russell WC (1987) Isolation and characterization of monoclonal antibodies to simian virus 5 and their use in revealing antigenic differences between human, canine and simian isolates. *J Gen Virol* 68(Pt 11):2769–2780.
40. Welch BD, et al. (2012) Structure of the cleavage-activated prefusion form of the parainfluenza virus 5 fusion protein. *Proc Natl Acad Sci USA* 109(41):16672–16677.
41. Zhang D, McCammon JA (2005) The association of tetrameric acetylcholinesterase with ColQ tail: A block normal mode analysis. *PLOS Comput Biol* 1(6):e62.
42. Luo J, Bruice TC (2002) Ten-nanosecond molecular dynamics simulation of the motions of the horse liver alcohol dehydrogenase.PhCH2O- complex. *Proc Natl Acad Sci USA* 99(26):16597–16600.
43. Young MA, Gonfloni S, Superti-Furga G, Roux B, Kuriyan J (2001) Dynamic coupling between the SH2 and SH3 domains of c-Src and Hck underlies their inactivation by C-terminal tyrosine phosphorylation. *Cell* 105(1):115–126.
44. Gkeka P, Papafotika A, Christoforidis S, Cournia Z (2015) Exploring a non-ATP pocket for potential allosteric modulation of PI3Kα. *J Phys Chem B* 119(3):1002–1016.
45. Apte-Sengupta S, et al. (2012) Base of the measles virus fusion trimer head receives the signal that triggers membrane fusion. *J Biol Chem* 287(39):33026–33035.
46. Avila M, et al. (2015) Canine distemper virus envelope protein interactions modulated by hydrophobic residues in the fusion protein globular head. *J Virol* 89(2):1445–1451.
47. Li J, Quinlan E, Mirza A, Iorio RM (2004) Mutated form of the Newcastle disease virus hemagglutinin-neuraminidase interacts with the homologous fusion protein despite deficiencies in both receptor recognition and fusion promotion. *J Virol* 78(10): 5299–5310.
48. Corti D, et al. (2013) Cross-neutralization of four paramyxoviruses by a human monoclonal antibody. *Nature* 501(7467):439–443.
49. Connolly SA, Leser GP, Jardetzky TS, Lamb RA (2009) Bimolecular complementation of paramyxovirus fusion and hemagglutinin-neuraminidase proteins enhances fusion: Implications for the mechanism of fusion triggering. *J Virol* 83(21): 10857–10868.
50. Bose S, et al. (2013) Mutations in the parainfluenza virus 5 fusion protein reveal domains important for fusion triggering and metastability. *J Virol* 87(24):13520–13531.
51. Welch BD, et al. (2014) Probing the functions of the paramyxovirus glycoproteins F and HN with a panel of synthetic antibodies. *J Virol* 88(20):11713–11725.
52. Paterson RG, Lamb RA (1993) The molecular biology of influenza viruses and paramyxoviruses. *Molecular Virology: A Practical Approach*, eds Davidson A, Elliott RM (IRL Oxford Univ Press, Oxford), pp 35–73.
53. Schrodinger L (2010) The PyMOL Molecular Graphics System, Version 1.3r1. Available at pymol.org/edu/?q=educational. Accessed June 11, 2016.
54. Schafmeister CEAF, Ross WS, Romanovski V (1995) LEaP. (University of California, San Francisco).
55. Phillips JC, et al. (2005) Scalable molecular dynamics with NAMD. *J Comput Chem* 26(16):1781–1802.
56. Hornak V, et al. (2006) Comparison of multiple Amber force fields and development of improved protein backbone parameters. *Proteins* 65(3):712–725.
57. Jorgensen JL, Chandrasekhar J, Madura JD, Impey RW, Klein ML (1983) Comparison of simple potential functions for simultating liquid water. *J Chem Phys* 79(2):926–935.
58. Piana S, et al. (2012) Evaluating the effects of cutoffs and treatment of long-range electrostatics in protein folding simulations. *PLoS One* 7(6):e39918.
59. Cunningham MA (2012) Dynamical probing of allosteric control in nuclear receptors. *J Mol Model* 18(7):3147–3152.
60. Hess B (2002) Convergence of sampling in protein simulations. *Phys Rev E Stat Nonlin Soft Matter Phys* 65(3 Pt 1):031910.